Acta Crystallographica Section A
Foundations of Crystallography
ISSN 0108-7673

Received 20 May 2008
Accepted 9 July 2008

Determination of the electrostatic potential and electron density of silicon using convergent-beam electron diffraction

Yoichiro Ogata, Kenji Tsuda* and Michiyoshi Tanaka

Institute of Multidisciplinary Research for Advanced Materials, Tohoku University, Sendai 980-8577, Japan. Correspondence e-mail: k_tsuda@tagen.tohoku.ac.jp

A structure-analysis method using convergent-beam electron diffraction (CBED) developed by Tsuda *et al.* [Tsuda & Tanaka (1999), *Acta Cryst.* A**55**, 939–954; Tsuda, Ogata, Takagi, Hashimoto & Tanaka (2002), *Acta Cryst.* A**58**, 514–525] has been applied to the determination of the electrostatic potential and electron density of crystalline silicon. CBED patterns recorded at nine different incidences are simultaneously used to improve the accuracy of the refinement. The Debye–Waller factor and low-order structure factors of silicon have been successfully refined only using CBED data. The electrostatic potential and electron-density distribution have been reconstructed from the refined parameters. The latter clearly shows the bonding electrons between the nearest neighbor atoms. The obtained results are compared with the results of other CBED and recent X-ray diffraction experiments. The influence of the number of refined low-order structure factors on the electron density is discussed. The effect of the reduction of experimental data points on the accuracy of the refined parameters is also examined.

© 2008 International Union of Crystallography
Printed in Singapore – all rights reserved

1. Introduction

The most common method used for the determination of electron-density distributions of crystalline specimens is X-ray diffraction. However, strong low-order reflections of X-ray diffraction, which are crucial for obtaining the distribution of valence electrons, are often subjected to the extinction effect owing to multiple scattering. This effect is serious, especially for the electron-density analysis of inorganic materials. This problem can be overcome by convergent-beam electron diffraction (CBED), which allows us to determine accurately the structure factors of low-order reflections (low-order structure factors) while fully taking account of the multiple scattering (*e.g.* Spence & Zuo, 1992; Spence, 1993).

Refinements of low-order structure factors using convergent-beam electron diffraction (CBED) patterns have been reported by many researchers. Spence & Zuo (1992) demonstrated such an analysis using one-dimensional line profiles of an energy-filtered CBED pattern recorded under systematic diffraction conditions. Zuo *et al.* (1999) determined low-order structure factors of Cu_2O using their approach. They reconstructed the electron-density distribution with the combined use of the low-order structure factors determined by them and other high-order structure factors measured using X-rays. Similar reconstruction of the electron-density distribution was carried out for TiO_2 (Jiang *et al.*, 2003), $SrTiO_3$ (Friis *et al.*, 2004) and Cu (Friis *et al.*, 2005). These results are also summarized in a review by Zuo (2004). Bird & Saunders (1992) proposed an approach using two-dimensional intensities of a CBED pattern recorded at a zone-axis or a near-zone-axis condition. Since two-dimensional CBED intensities provide much more information on structural parameters, more parameters can be refined with a high accuracy from a single CBED pattern. Low-order structure factors of Si (Saunders *et al.*, 1999*a*,*b*) and Ni and Cu (Saunders *et al.*, 1999*a*,*b*) were determined using two-dimensional zone-axis CBED patterns. The electron-density distribution of Al_2O_3 was also determined with the combined use of the two-dimensional CBED zone-axis pattern and synchrotron X-ray diffraction by Streltsov *et al.* (2003).

In all the above analyses, only zeroth-order Laue zone (ZOLZ) reflections at low scattering angles were used because of the instrumental limitation of the energy filters. Since such ZOLZ reflections are not so sensitive to atom positions and Debye–Waller factors, these parameters needed to be accurately determined by X-rays. It should be noted that accurate values of the atom positions and Debye–Waller factors are also necessary in the course of the conversion from the structure factors for electrons to those for X-rays, which are necessary to obtain the electron-density distribution.

Tsuda & Tanaka (1999) extended the method to use two-dimensional intensities of not only ZOLZ reflections but also higher-order Laue zone (HOLZ) reflections of CBED patterns. For this purpose, an in-column-type energy-filter transmission electron microscope which can record diffraction patterns up to a high angle with small distortion, and analysis

software to treat ZOLZ and HOLZ reflection discs, were developed (Tsuda & Tanaka, 1999; Tanaka *et al.*, 1999). The use of HOLZ reflections is essential for determining small displacements of atoms because HOLZ reflections with large reciprocal vectors are sensitive to those displacements. The simultaneous use of ZOLZ and HOLZ reflections allows us to accurately determine atom positions, Debye–Waller factors (atomic displacement parameters) and the low-order structure factors, all of which are the parameters required to calculate the electron-density distribution (Tsuda *et al.*, 2002). Thus, true nanometer-scale local structure analysis can be accomplished using our technique. That is, the electron-density distribution can be determined only from the CBED data without any help from X-ray data. Tsuda *et al.* (2002) applied this method to the rhombohedral phase of $LaCrO_3$ and determined its atom positions, anisotropic Debye–Waller factors and low-order structure factors. Ogata *et al.* (2004) determined 21 parameters of atom positions and Debye–Waller factors of the orthorhombic phase of hex-$BaTiO_3$ from CBED patterns using this method.

The present paper is intended to apply the method developed by Tsuda & Tanaka (1999) to the determination of the electrostatic potential and electron-density distribution of crystalline silicon. The Debye–Waller factor and low-order structure factors of silicon are refined using only intensity data from CBED patterns, and the electrostatic potential and electron-density distribution are reconstructed from the refined parameters. The present results are compared with the results of other CBED and recent X-ray diffraction experiments. The capabilities and limitations of the method are examined. The influence of the number of refined low-order structure factors on the resultant electron-density distribution is discussed. The effect of the reduction of experimental data points on the accuracy of the refined parameters is also examined.

2. Experimental method and analysis procedure

The CBED experiments were conducted using a JEM-2010FEF transmission electron microscope equipped with a Schottky-type field-emission gun and an in-column Ω-type energy filter which can remove inelastically scattered electrons (Tsuda & Tanaka, 1999; Tanaka *et al.*, 1999). This microscope can take energy-filtered CBED patterns with a high acceptance angle of about 10°, which corresponds to a lattice spacing of 0.21 Å, at an accelerating voltage of 100 kV and an acceptance energy width of ± 10 eV. Single-crystal silicon specimens for the CBED experiments were prepared by mechanical thinning and subsequent Ar ion thinning. Energy-filtered CBED patterns were recorded at the [111] and [110] zone-axis incidences and at the Bragg conditions of low-order reflections near the [111] and [110] incidences. It is expected that the CBED pattern recorded at the Bragg condition of a reflection has higher sensitivity to the structure factor of the reflection. The CBED patterns were recorded from specimen areas of a few nanometers in diameter at room temperature with an acceptance energy width of 0 ± 10 eV. The intensities of the CBED patterns were recorded on imaging plates and were subsequently read out using an imaging-plate reader, DITABIS micron, with a 20-bit dynamic range. The accelerating voltage of the microscope was determined to be 100.9 (2) kV from the HOLZ line positions of the [111] zone-axis CBED pattern.

The raw experimental data are corrected in the following two ways (Tsuda & Tanaka, 1999). The distortions of the CBED patterns owing to the aberration of the lenses and the energy filter were corrected using the analytical equations of the distortions with the distortion coefficients determined from the positions of the reflection discs. The remaining weak background intensities owing to thermal diffuse scattering in each disc were subtracted by interpolating background intensities just outside the CBED disc in the direction of the nearest Kikuchi line or band.

The structural parameters are refined by a non-linear least-squares fitting so as to minimize the residual sum of squares χ^2 between the experimental CBED intensities and theoretical ones. χ^2 is defined as

$$\chi^2 = \sum_i w_i \left[I_i^{\rm exp} - s I_i^{\rm cal}(\mathbf{x}, t) \right]^2 \tag{1}$$

for a CBED pattern, where $I_i^{\rm exp}$ is the ith intensity of the experimental data corrected as described above, $I_i^{\rm cal}(\mathbf{x}, t)$ is the intensity calculated based on the dynamical diffraction theory, $\mathbf{x}$ stands for structural parameters and t is a specimen thickness, w_i is a weight factor and s is a scale factor common to the calculated intensities of the CBED pattern. The CBED patterns recorded at different incidences are simultaneously used for the refinement, where the sum of χ^2 for the CBED patterns is minimized.

The weight factor for the ith intensity is set to $w_i = w_{\rm LZ}/(\sigma_i^{\rm exp})^2$, where $\sigma_i^{\rm exp}$ is the experimental error of $I_i^{\rm exp}$ evaluated by assuming a Poisson distribution. $w_{\rm LZ}$ is an additional weight factor to decrease the contribution of ZOLZ reflections to the refinement of the atom positions and Debye–Waller factors. The factor is necessary because the intensities of the ZOLZ reflections are typically 10^2 times greater than those of the HOLZ reflections. $w_{\rm LZ}$ for ZOLZ reflections is determined so as to satisfy the relation

$$w_{\rm LZ} \sum_{\rm ZOLZ} \left(I_i^{\rm exp} / \sigma_i^{\rm exp} \right)^2 = \sum_{\rm HOLZ} \left(I_i^{\rm exp} / \sigma_i^{\rm exp} \right)^2, \tag{2}$$

but $w_{\rm LZ}$ for HOLZ reflections is set to 1.0. In the present analysis, $w_{\rm LZ}$ for the ZOLZ reflections of the [111] patterns was set to 0.179. $w_{\rm LZ}$ for those of the [110] patterns was set to 1.0 because no HOLZ reflection appeared in the [110] patterns.

Structural parameters $\mathbf{x}$ to be refined consist of atom positions, Debye–Waller factors (atomic displacement parameters), crystal structure factors for electrons $F_{\mathbf{g}}^{\rm e}$ and absorption coefficients $F_{\mathbf{g}}^{\rm e\prime}$ of low-order reflections. In the diamond structure of silicon with space group $Fd\bar{3}m$, the positional parameter to be refined is only the isotropic Debye–Waller factor B of an Si atom. All the atoms are fixed to the Wyckoff position 8*a* with site symmetry $\bar{4}3m$ and the compo-

nents of the anisotropic Debye–Waller factors of the atoms are related by $U_{11} = U_{22} = U_{33}$ and $U_{12} = U_{23} = U_{13} = 0$. The values of $F^{\rm e}_{\bf g}$ of the higher-order reflections other than those to be refined are calculated by assuming the independent-atom model (IAM), or are calculated using the electron atomic scattering factors for the neutral atom from the Doyle & Turner expression (Doyle & Turner, 1968). The values of $F^{\rm e\prime}_{\bf g}$ are evaluated using the absorption form factors owing to thermal diffuse scattering (Hall & Hirsch, 1965). The atomic scattering factors and the absorption form factors are calculated by the subroutine *ATOM* of Bird & King (1990). The lattice parameter 5.4310 Å at room temperature was used for the present analysis (Becker *et al.*, 1982).

The scale factor and specimen thickness are refined together with the structural parameters. The geometrical parameters of the reflections, which are the factors that precisely adjust the positions of the CBED discs, are also refined separately from the other parameters to eliminate the influence of correlations between the geometrical parameters and the structural parameters. The refinements of the parameters are carried out using the analysis software *MBFIT* (Tsuda & Tanaka, 1999; Tsuda *et al.*, 2002), which is based on the Bloch-wave formulation of the dynamical diffraction theory (*e.g.* Spence & Zuo, 1992) and Fletcher's modified Marquard method of non-linear least-squares fitting (Fletcher, 1971). The calculations were performed on a 16-node Linux PC cluster composed of AMD Opteron CPUs using the modified version of *MBFIT* which has the function of parallel computation (Ogata *et al.*, 2004).

The electrostatic potential $V({\bf r})$ and electron density $\rho({\bf r})$ are calculated from the refined values of the atom positions, Debye–Waller factors and low-order structure factors. The electrostatic potential $V({\bf r})$ is directly obtained by the Fourier synthesis

$$V({\bf r}) = \sum_{\bf g} V_{\bf g} \exp(2\pi i {\bf g}\cdot{\bf r}). \qquad (3)$$

The Fourier coefficients $V_{\bf g}$ are proportional to the structure factors for electrons $F^{\rm e}_{\bf g}$, $V_{\bf g} = F^{\rm e}_{\bf g} h^2/(8\pi\varepsilon_0 m_{\rm e} e^2 \Omega)$, where h, ε_0, $m_{\rm e}$, e and Ω are Planck's constant, the dielectric constant of a vacuum, the rest mass of an electron, the charge of an electron and the volume of the unit cell, respectively.

The Fourier coefficients of the electrostatic potential $V_{\bf g}$ are converted to the structure factors for X-rays $F^{\rm X}_{\bf g}$, using the relation derived from Poisson's equation (Spence & Zuo, 1992),

$$\begin{aligned} F^{\rm X}_{\bf g} = & -\left(16\pi^2\varepsilon_0\Omega/|e|\right)s^2 V_{\bf g} \\ & + \sum_j Z_j \exp(-B_j s^2)\exp\left(-2\pi i {\bf g}\cdot{\bf r}_j\right), \end{aligned} \qquad (4)$$

where $s = \sin\theta/\lambda = |{\bf g}|/2$, Z_j is the atomic number of the jth atom, B_j is the Debye–Waller factor of the jth atom and ${\bf r}_j$ is the position of the jth atom. It should be noted that the Debye–Waller factor is included in the second term of equation (4) to describe the contribution of the nuclear charge. Thus, the value of the Debye–Waller factor is crucial in obtaining accurate low-order $F^{\rm X}_{\bf g}$ from $V_{\bf g}$. We emphasize that the factors can be accurately determined in the present analysis because both ZOLZ and HOLZ reflections are available. The electron density $\rho({\bf r})$ is obtained by the Fourier synthesis

$$\rho({\bf r}) = (1/\Omega)\sum_{\bf g} F^{\rm X}_{\bf g} \exp(2\pi i {\bf g}\cdot{\bf r}). \qquad (5)$$

The three-dimensional distributions of the electrostatic potential and electron density are visualized by the software *VESTA*, developed by Momma & Izumi (2008).

3. Results

3.1. Refinement of the Debye–Waller factor

The Debye–Waller factor of an Si atom at room temperature was determined from the [111] CBED patterns containing ZOLZ and the first-order Laue zone (FOLZ) reflections. Figs. 1(*a*) and 1(*b*) show, respectively, the patterns recorded at the [111] zone-axis incidence and at the Bragg condition of the $2\bar{2}0$ reflection near the [111] incidence. The thicknesses of their specimen areas were ~85 nm and ~103 nm, respectively. After the distortion correction and background subtraction, 22 reflections were selected for fitting from the zone-axis

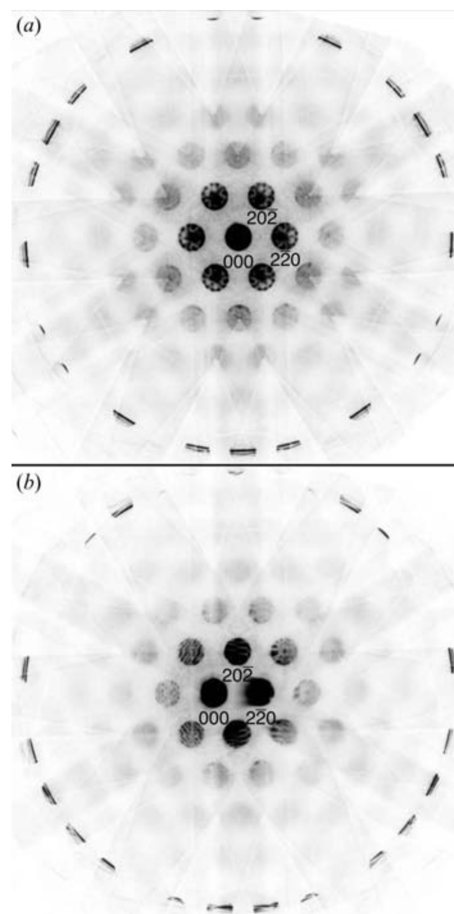

Figure 1
Energy-filtered CBED patterns recorded at (*a*) the [111] zone-axis incidence and (*b*) the Bragg condition of the $2\bar{2}0$ reflection near the [111] zone axis.

pattern of Fig. 1(*a*), and 17 reflections from the $2\bar{2}0$-excited pattern of Fig. 1(*b*), where the numbers of raw data points were 11 6025 and 82 785, respectively. The FOLZ reflections have high enough indices to determine the Debye–Waller factor precisely. One-sixteenth of the raw data were used for the refinements. The Debye–Waller factor B was refined with the combined use of the two CBED patterns.

The reflections with excitation errors $s_{\mathbf{g}} < 1.0$ Å^{-1} were used for the dynamical calculations and those with $0.5 \leq s_{\mathbf{g}} < 1.0$ Å^{-1} were treated by the generalized Bethe potential (GBP) method (Ichikawa & Hayakawa, 1977). The number of selected reflections was 376 (102) for the zone-axis pattern and 385 (117) for the $2\bar{2}0$ Bragg pattern, where the numbers in parentheses are those treated by the GBP method.

In order to eliminate the errors owing to the correlation between the Debye–Waller factor and the low-order structure factors and absorption coefficients, the refinements were alternately repeated in the following manner. The Debye–Waller factor was first refined using the IAM values for the low-order structure factors and absorption coefficients. The refined Debye–Waller factor was subsequently used to refine the low-order structure factors and absorption coefficients, as described in the next section. Then, using the refined values of the low-order structure factors and absorption coefficients, the Debye–Waller factor was refined again. This process was repeated twice.

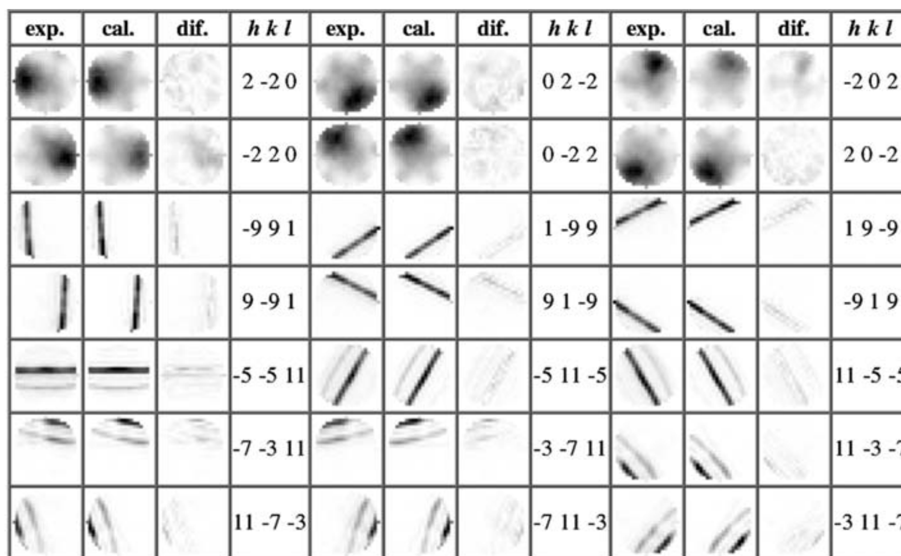

(*a*)

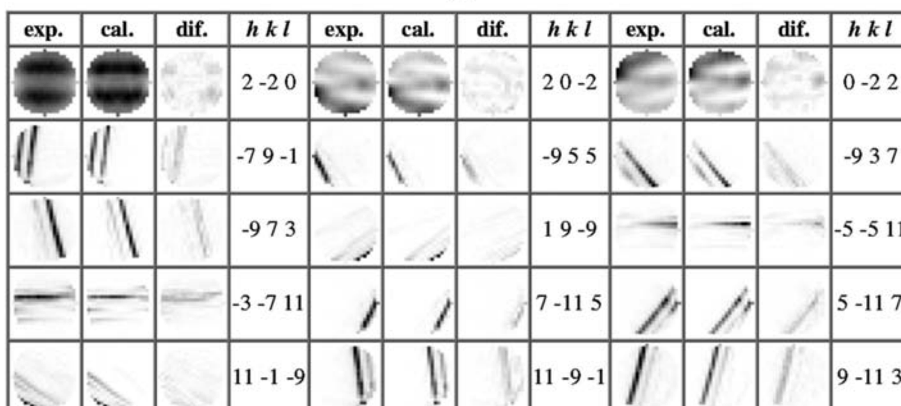

(*b*)

Figure 2
Final results of the fitting of (*a*) the [111] zone-axis pattern and (*b*) the $2\bar{2}0$ Bragg pattern. The patterns in the left, center and right columns show experimental, calculated and difference patterns, respectively.

Figs. 2(*a*) and 2(*b*) show, respectively, the final results of the fitting of the zone-axis pattern and the $2\bar{2}0$ Bragg pattern. The patterns in the left, center and right columns show, respectively, the experimental, calculated and difference patterns of the CBED discs. The calculated patterns are seen to agree well with the experimental patterns. The value of the Debye–Waller factor was determined to be B = 0.463 (1) Å^2 by averaging the results of the fittings which used five data sets extracted from the same CBED patterns with different pixel sampling. The number in parentheses shows the standard deviation of the last digit which was evaluated from the five fittings.

3.2. Refinement of the low-order structure factors

The low-order structure factors sensitive to valence electrons were determined from the ZOLZ reflections of the [110] CBED patterns because the patterns contain all of the low-order structure factors to be refined. The nine CBED patterns recorded at the $\bar{1}11$, $\bar{2}20$, $\bar{1}13$, $\bar{2}22$, 004, $\bar{3}31$, $\bar{2}24$, $\bar{1}15$ and $\bar{3}33$ Bragg conditions near the [110] incidence were simultaneously used for the refinements, which are shown in Figs. 3(*a*)–3(*i*). In the present analysis the structure factors $F^{\rm e}_{\mathbf{g}}$ and absorption coefficients $F^{\rm e\prime}_{\mathbf{g}}$ of the 111, 220, 311, 222, 400, 331 and 422 reflections with $\sin\theta/\lambda \leq 0.451$ Å^{-1} were refined. The thicknesses of the specimen areas were approximately 180 nm.

After the distortion corrections and background subtractions, 9, 13, 9, 8, 12, 9, 13, 11 and 11 reflections were selected for the fitting from the patterns of the $\bar{1}10$, $\bar{2}20$, $\bar{1}13$, $\bar{2}22$, 004, $\bar{3}31$, $\bar{2}24$, $\bar{1}15$ and $\bar{3}33$ Bragg conditions, respectively, where the numbers of raw data points were 48 492, 70 044, 48 492, 43 104, 64 656, 48 492, 70 044, 59 268 and 59 268, respectively. One-sixteenth of the raw data were used for the refinements.

The reflections with excitation errors $s_{\mathbf{g}} < 1.0$ Å^{-1} were used for the dynamical calculations but those with $0.5 \leq s_{\mathbf{g}} < 1.0$ Å^{-1} were treated by the GPB method. The numbers of

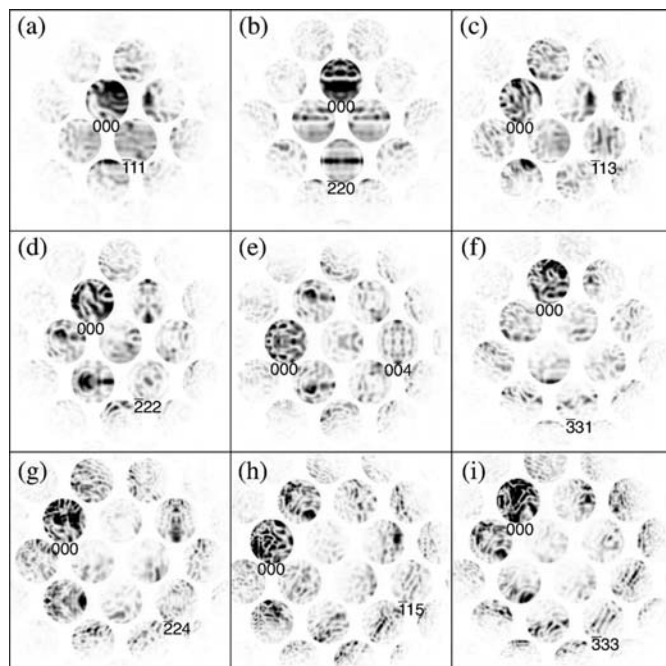

Figure 3
Energy-filtered CBED patterns recorded at the (*a*) $\bar{1}11$, (*b*) $\bar{2}20$, (*c*) $\bar{1}13$, (*d*) $\bar{2}22$, (*e*) 004, (*f*) $\bar{3}31$, (*g*) $\bar{2}24$, (*h*) $\bar{1}15$ and (*i*) $\bar{3}33$ Bragg conditions near the [110] incidence.

selected reflections were 382 (186), 384 (182), 384 (185), 389 (185), 391 (186), 386 (184), 386 (182), 391 (184) and 390 (184), respectively, for the patterns recorded at the $\bar{1}10$, $\bar{2}20$, $\bar{1}13$, $\bar{2}22$, 004, $\bar{3}31$, $\bar{2}24$, $\bar{1}15$ and $\bar{3}33$ Bragg conditions, where the numbers in the parentheses refer to those treated by the GBP method.

Figs. 4(*a*) to 4(*i*) show the final results of the fitting of the patterns recorded at the $\bar{1}10$, $\bar{2}20$, $\bar{1}13$, $\bar{2}22$, 004, $\bar{3}31$, $\bar{2}24$, $\bar{1}15$ and $\bar{3}33$ Bragg conditions. The pattern in the left, center and right columns show experimental, calculated and difference patterns, respectively. The calculated patterns are seen to show excellent agreement with the experimental patterns. Similarly to the refinement of the Debye–Waller factor, the values of $F^{e}_{\mathbf{g}}$ and $F^{e\prime}_{\mathbf{g}}$ were determined by averaging the results of the fittings which used five data sets taken from the same CBED patterns by different pixel sampling. The refined values of $F^{e}_{\mathbf{g}}$ and $F^{e\prime}_{\mathbf{g}}$ were converted to the values of Fourier coefficients $V_{\mathbf{g}}$ and $V'_{\mathbf{g}}$ of the electrostatic potential, which are shown in Table 1 together with the values of the IAM of a neutral Si atom. The numbers in parentheses in Table 1 are the standard deviations evaluated from the five fittings.

3.3. Reconstruction of the electrostatic potential, absorption potential and electron density

The electrostatic potential $V_{\rm present}(\mathbf{r})$ was reconstructed using the Fourier synthesis of equation (3) from the refined values of the Debye–Waller factor and the low-order structure factors, and the IAM values for the high-order structure factors in the range 0.451 Å^{-1} < $\sin\theta/\lambda$ < 6.0 Å^{-1}. Fig. 5(*a*) shows the 12.0 V isosurface of the electrostatic potential

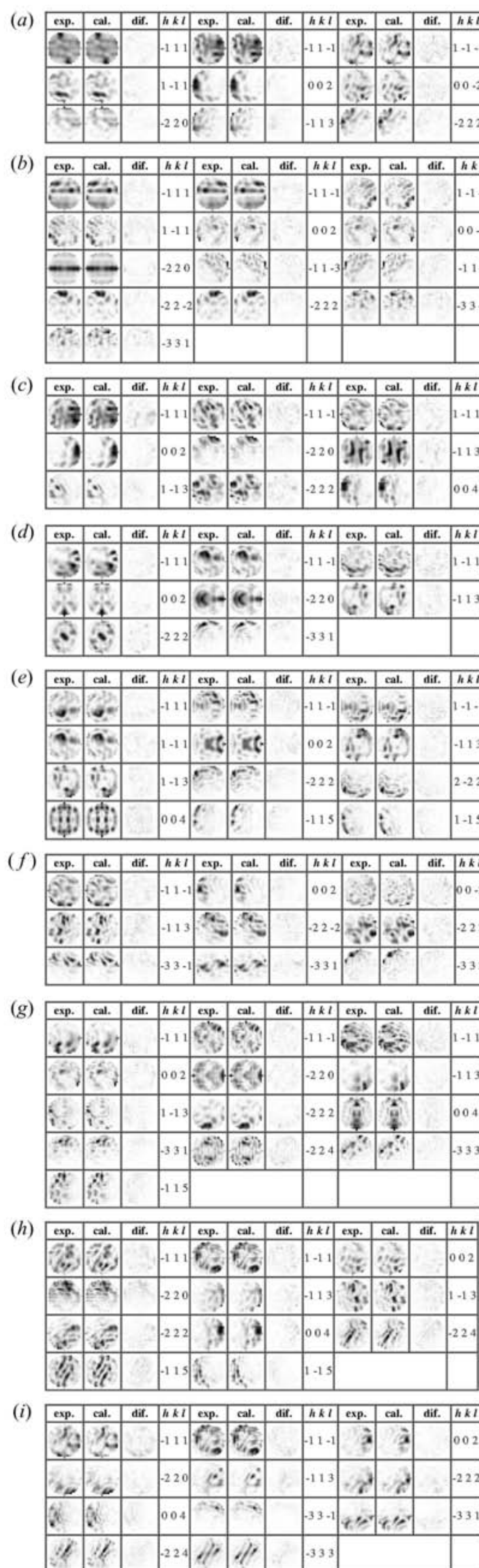

Figure 4
Final results of the fitting of the patterns of the (*a*) $\bar{1}11$, (*b*) $\bar{2}20$, (*c*) $\bar{1}13$, (*d*) $\bar{2}22$, (*e*) 004, (*f*) $\bar{3}31$, (*g*) $\bar{2}24$, (*h*) $\bar{1}15$ and (*i*) $\bar{3}33$ Bragg conditions near the [110] incidence. The patterns in the left, center and right columns show experimental, calculated and difference patterns, respectively.

Table 1
Fourier coefficients $V_{\mathbf{g}}$ and $V'_{\mathbf{g}}$ of the electrostatic potential and absorption potential converted from the refined $F^{\rm e}_{\mathbf{g}}$ and $F^{\rm e\prime}_{\mathbf{g}}$, and those of the IAM of a neutral Si atom.

	IAM	Present result
$V(111)$	−5.4481	−5.1542 (6)
$V(220)$	−4.3201	−4.3476 (12)
$V(311)$	−2.4236	−2.4743 (7)
$V(222)$	0.0000	−0.1073 (6)
$V(400)$	−2.5709	−2.5847 (11)
$V(331)$	1.5885	1.5530 (11)
$V(422)$	1.8668	1.8250 (10)
$V'(111)$	−0.0751	−0.1041 (2)
$V'(220)$	−0.0981	−0.1361 (5)
$V'(311)$	−0.0664	−0.0890 (4)
$V'(222)$	0.0000	−0.0080 (5)
$V'(400)$	−0.0883	−0.1039 (10)
$V'(331)$	0.0601	0.0663 (5)
$V'(422)$	0.0800	0.0867 (19)

$V_{\rm present}(\mathbf{r})$ obtained in the present analysis. The electrostatic potential of the IAM, $V_{\rm IAM}(\mathbf{r})$, is shown in Fig. 5(*b*) for comparison. Figs. 6(*a*) and 6(*b*) show the $(1\bar{1}0)$ sections of $V_{\rm present}(\mathbf{r})$ and $V_{\rm IAM}(\mathbf{r})$, respectively. The value of $V_{\rm present}(\mathbf{r})$ at the midpoint between the nearest Si atoms is 11.5 V, while that of $V_{\rm IAM}(\mathbf{r})$ is 14.6 V. This indicates that excess electrons or bonding electrons exist between the nearest atoms and decrease the potential level.

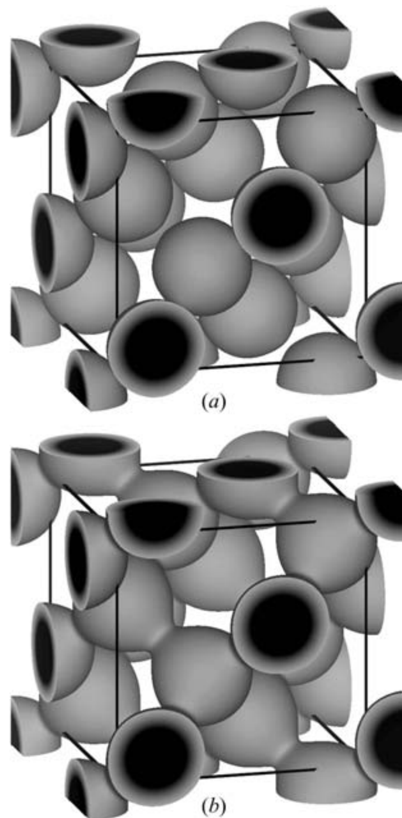

Figure 5
Three-dimensional visualization of (*a*) the electrostatic potential obtained in the present analysis and (*b*) that of the IAM, where the 12 V isosurface is shown. The unit cell is drawn with solid lines.

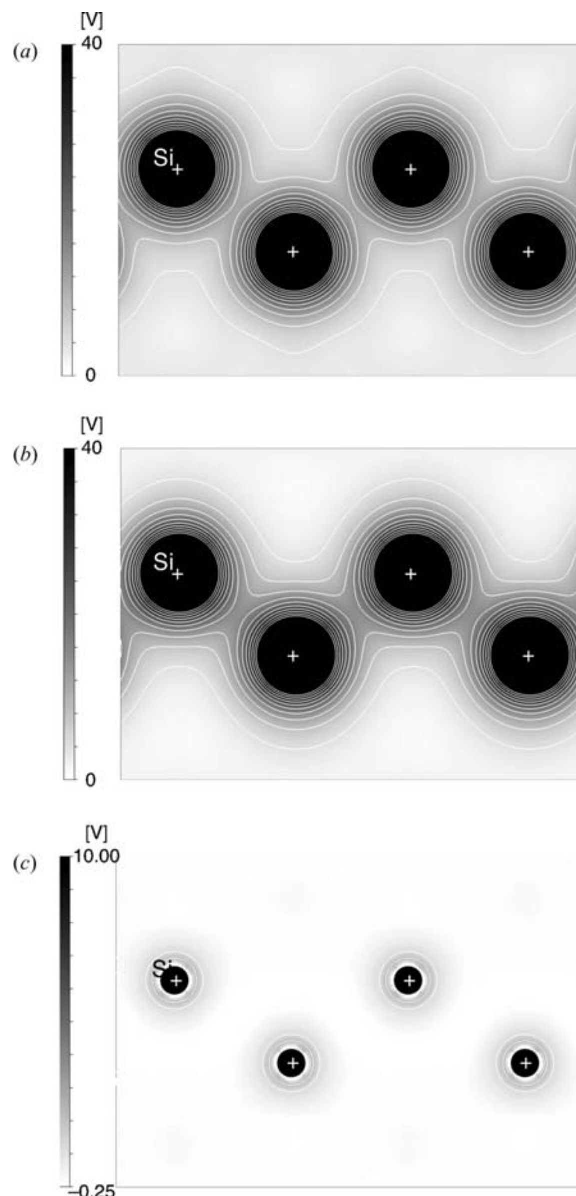

Figure 6
The $(1\bar{1}0)$ section of (*a*) the electrostatic potential obtained in the present analysis, (*b*) that of the IAM, and (*c*) the obtained absorption potential. The intervals of the contour lines of (*a*), (*b*) and (*c*) are 4.0 V, 4.0 V and 1.0 V, respectively.

The absorption potential $V'(\mathbf{r})$ was similarly calculated from the refined $V'_{\mathbf{g}}$. Fig. 6(*c*) shows the $(1\bar{1}0)$ section of the absorption potential obtained in the present analysis. The high absorption regions are seen to be confined to the atom sites.

The refined values of the low-order structure factors for electrons were converted to those of the structure factors for X-rays using equation (4). The electron density was calculated from the refined low-order structure factors using equation (5), where the IAM values were used for the high-order structure factors in the range $0.451\ \text{Å}^{-1} < \sin\theta/\lambda < 6.0\ \text{Å}^{-1}$. Fig. 7(*a*) shows the $0.45\ {\rm e}\ \text{Å}^{-3}$ isosurface of the present analysis, $\rho_{\rm present}(\mathbf{r})$. The bonding electrons are clearly seen in the positions between the nearest Si atoms. The electron density of the IAM, $\rho_{\rm IAM}(\mathbf{r})$, is shown in Fig. 7(*b*) for

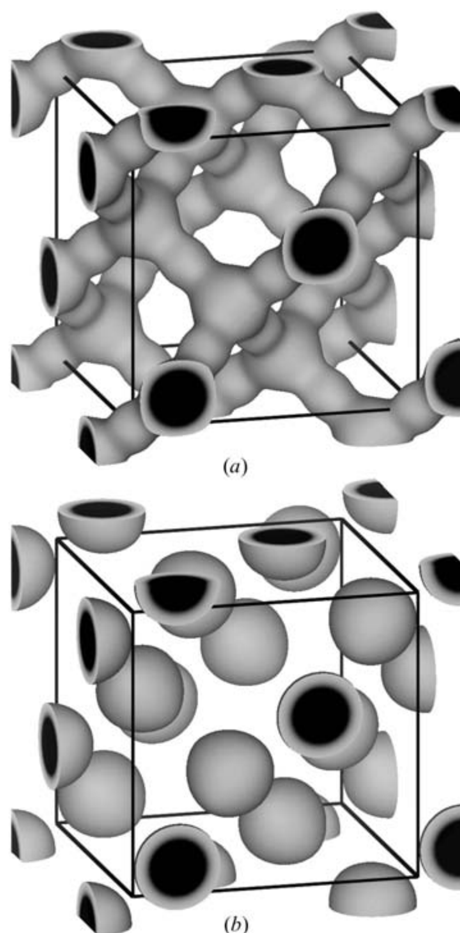

Figure 7
Three-dimensional visualization of (*a*) the electron density obtained in the present analysis and (*b*) that of the IAM, where the 0.45 e Å^{-3} isosurface is shown. The unit cell is drawn with solid lines.

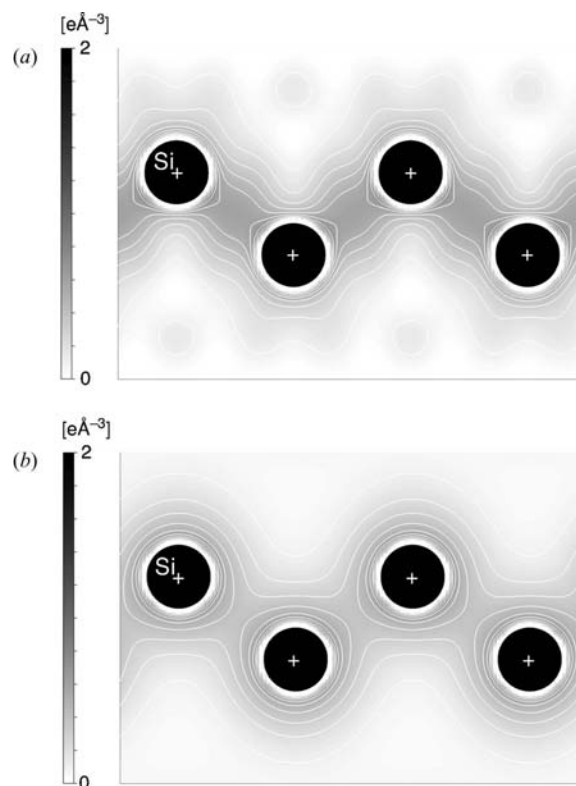

Figure 8
The (1$\bar{1}$0) section of (*a*) the electron density obtained in the present analysis and (*b*) that of the IAM. The interval of the contour lines is 0.1 e Å^{-3}.

comparison. Figs. 8(*a*) and 8(*b*) show the (1$\bar{1}$0) sections of $\rho_{\rm present}(\mathbf{r})$ and $\rho_{\rm IAM}(\mathbf{r})$, respectively. The value of $\rho_{\rm present}(\mathbf{r})$ at the midpoint between the nearest Si atoms is 0.60 e Å^{-3}, which is notably higher than that of $\rho_{\rm IAM}(\mathbf{r})$ of 0.38 e Å^{-3}.

The standard deviation of the electron density $\rho_{\rm present}(\mathbf{r})$ was calculated according to the formalism of Rees (1978) from the evaluated standard deviations of the Debye–Waller factor and the low-order structure factors. The value of the standard deviation at the midpoint between the nearest Si atoms was 0.03 e Å^{-3}.

4. Discussion

4.1. Comparison with other experimental results

The results obtained in the present analysis are compared with other results of CBED and X-ray diffraction experiments. Spackman (1986) determined the Debye–Waller factor of silicon to be B = 0.4632 (11) Å^2 based on a multipole refinement using the data from X-ray *pendellösung* experiments of Aldred & Hart (1973) and Teworte & Bonse (1984). Zuo *et al.* (1997) obtained the Debye–Waller factor of B = 0.4668 (6) Å^2 from the comparison between multi-configurational Dirac–Fock calculations and the X-ray *pendellösung* data of Cummings & Hart (1988) and Saka & Kato (1986). Yamamoto *et al.* (1996) reported the Debye–Waller factor B = 0.467 (1) Å^2 from single-crystal X-ray diffraction experiments using short-wavelength X-rays of W $K\alpha_1$. The value obtained by the present analysis, B = 0.463 (1) Å^2, at room temperature closely agrees with these values though it is closer to the value of Spackman (1986).

The values of the refined low-order crystal structure factors for X-rays in the present analysis are shown in Table 2. The table also contains the values obtained by Saka & Kato (1986) using the X-ray *pendellösung* fringe method; by Cummings & Hart (1988), which are the averaged values of the X-ray *pendellösung* experiments of Aldred & Hart (1973), Teworte & Bonse (1984) and Saka & Kato (1986); by Nishibori *et al.* (2007) using synchrotron powder X-ray diffraction at SPring-8, by Saunders *et al.* (1995) and Saunders *et al.* (1996) using a zone-axis ZOLZ CBED pattern and a 002 Bragg pattern; and by Deininger *et al.* (1995) using line profiles of ZOLZ CBED patterns recorded under systematic conditions. It is noted that Yamamoto *et al.* (1996) did not present the values of the structure factors in their paper. The values of the present analysis are seen to be close to those of Saka & Kato (1986) and Nishibori *et al.* (2007), though the value of F(422) of the present analysis is slightly larger than their values, in which the Fourier truncation error might be included. Although the data of Saka & Kato (1986) have been known to be highly accurate, the value of the 222 reflection is lacking, which has a great

Table 2
Low-order structure factors for X-rays refined in the present analysis, together with those obtained from other CBED and X-ray diffraction experiments.

The values were converted to those at room temperature using the Debye–Waller factor.

	IAM	Present result	Saka & Kato (1986)	Cummings & Hart (1988)	Nishibori *et al.* (2007)	Saunders *et al.* (1995) (ZA)	Saunders *et al.* (1996) (002)	Deininger *et al.* (1995)
$F(111)$	−58.903	−59.948 (3)	−60.13 (5)	−59.98 (2)	−60.0 (1)	−59.963 (6)	−59.912 (6)	−59.30 (6)
$F(220)$	−67.588	−67.33 (1)	−67.34 (5)	−67.10 (2)	−67.2 (1)	−67.08 (4)	−67.11 (6)	−66.5 (1)
$F(311)$	−44.262	−43.60 (1)	−43.63 (3)	−43.45 (1)	−43.4 (1)	−43.4 (1)	−43.48 (4)	
$F(222)$	0	1.526 (9)		1.456 (8)	1.6 (3)	1.20 (8)	1.44 (8)	1.5 (2)
$F(400)$	−56.444	−56.18 (2)	−56.23 (4)	−55.97 (1)	−56.0 (2)	−55.8 (4)	−56.6 (4)	−50.6 (2)
$F(331)$	37.744	38.54 (3)	38.22 (3)	38.05 (1)	38.5 (1)	38.4 (3)	38.8 (5)	
$F(422)$	48.845	50.04 (3)	49.11 (4)	48.90 (2)	49.3 (1)			

contribution to the bonding electron density. The values of Nishibori *et al.* (2007) are close to those of Saka & Kato (1986) but their standard deviations are one order larger owing to powder diffraction experiments.

The values of $F(111)$, $F(220)$ and $F(400)$ by Deininger *et al.* (1995) deviate significantly from the other results, presumably because of the use of line profile data. Saunders *et al.* (1995) reported relatively large differences in the values of $F(222)$ and $F(400)$ between the two separate analyses of the zone-axis and 002 Bragg CBED patterns. On the other hand, in the present analysis reliable single values were obtained for them without such discrepancies because the analysis was performed by combining the CBED patterns recorded at nine different incidences. Since Saunders *et al.* (1995) and Deininger *et al.* (1995) conducted the CBED experiments at liquid-nitrogen temperature, they needed to use the Debye–Waller factors at the low temperature for the refinements of the structure factors. Saunders *et al.* (1995) used $B = 0.25$ Å^2, which was obtained using ZOLZ CBED patterns. Deininger *et al.* (1995) assumed $B = 0.27$ Å^2, which was taken from theoretical calculations. The structure factors obtained were converted to those at room temperature using a value of $B = 0.46$ Å^2 determined by X-rays. In the present analysis the CBED experiments were conducted at room temperature. The Debye–Waller factors and the low-order structure factors were simultaneously determined only from the CBED data. Thus, the error introduced by the Debye–Waller factor in the present case was much smaller than the errors in the case of Saunders *et al.* (1995) and Deininger *et al.* (1995).

The electron-density distributions were calculated by Spackman (1986) using Fourier synthesis and by Yamamoto *et al.* (1996) and Nishibori *et al.* (2007) based on the maximum entropy method. The values of the electron density at the midpoint between the nearest Si atoms reported by Spackman (1986), Yamamoto *et al.* (1996) and Nishibori *et al.* (2007) were 0.609 (6), 0.568 and 0.56 e Å^{-3}, respectively, where the number in parentheses is the standard deviation of the last digit. Yamamoto *et al.* (1996) and Nishibori *et al.* (2007) did not present the standard deviation. These values can be said to agree with the present value of 0.60 (3) e Å^{-3} almost within the standard deviation.

Zuo *et al.* (1997) presented difference electron-density maps from the IAM values for the experimental data of Cummings & Hart (1988) and Saka & Kato (1986) and a density functional calculation using the generalized gradient approximation. The difference values for the experimental and theoretical results at the midpoint are 0.213 (3) e Å^{-3} and 0.194 e Å^{-3}, respectively. The corresponding difference electron density in the present analysis is evaluated to be 0.22 (3) e Å^{-3}. Saunders *et al.* (1995) presented a smaller value of around 0.16 e Å^{-3} because the Fourier synthesis used only four structure factors.

4.2. The number of low-order structure factors to be refined

The accuracy of the electron-density distribution obtained is influenced by the number of low-order structure factors to be refined. The other high-order structure factors are set to the IAM values, introducing a bias to the electron density. In order to obtain accurate distributions of bonding electrons, it is essential to refine the low-order structure factors whose values deviate from their IAM values. It was found that deviations of the structure factors of the 333 and 511 reflections ($\sin\theta/\lambda = 0.478$ Å^{-1}) from their IAM values, which are the lowest-order reflections next to the 422 reflection ($\sin\theta/\lambda = 0.451$ Å^{-1}), did not improve the χ^2 values of the CBED patterns recorded at their Bragg conditions. Thus, the seven low-order structure factors up to the 422 reflection were refined in the present analysis.

For comparison, two additional refinements were performed for the five low-order structure factors up to the 400 reflection ($\sin\theta/\lambda = 0.368$ Å^{-1}) and for the six low-order structure factors up to the 331 reflection ($\sin\theta/\lambda = 0.401$ Å^{-1}). The reconstructions of electron density were performed using the low-order structure factors obtained, where the values of the high-order reflections were fixed to the IAM values. Fig. 9(*a*) shows the $(1\bar{1}0)$ section of the electron density obtained from the refinement of the five structure factors. The electron density is 0.52 e Å^{-3} at the midpoint between the nearest Si atoms. Fig. 9(*b*) shows the same section of the electron density obtained from the refinement of the six structure factors. The electron density is 0.62 e Å^{-3} at the midpoint. Bonding electrons are clearly seen in both Figs. 9(*a*) and 9(*b*). It was, however, found that the electron density at the midpoint was notably different between the refinement with the five structure factors and that with the six structure factors. It was also found that negative areas appear in the electron-density map of Fig. 9(*b*). These facts indicate that the

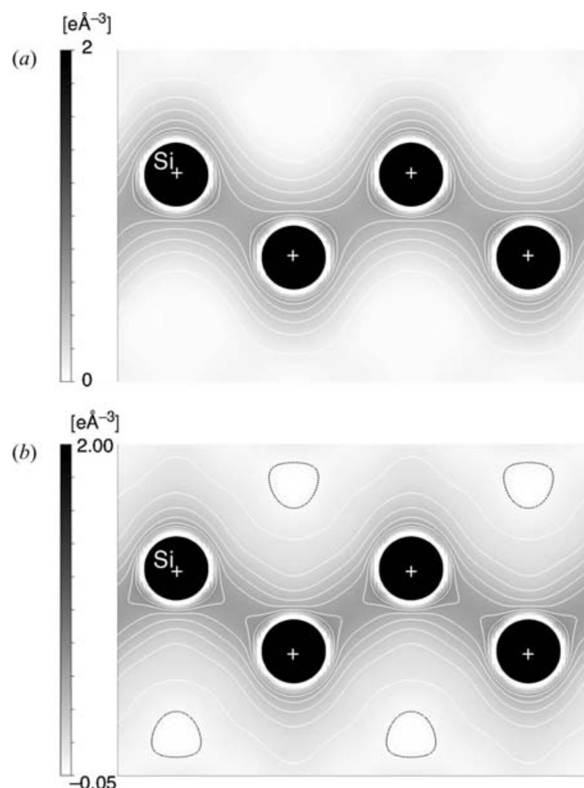

Figure 9
The $(1\bar{1}0)$ section of (*a*) the electron densities reconstructed from the five refined structure factors up to the 400 reflection and (*b*) that from the six refined ones up to the 331 reflection. The white and black contour lines indicate positive and negative values of the electron density, respectively.

refinements with the five and six low-order structure factors are not sufficient to obtain an accurate electron density. In the refinement with the seven structure factors, the negative areas of the electron density were almost removed with only a change of 0.02 e Å^{-3} at the midpoint in the electron density as seen in Fig. 8(*a*). Thus, in the present analysis, we have concluded that the refinement of the seven low-order structure factors up to the 422 reflection is the most reliable. It is noted that Saunders *et al.* (1995) used only four low-order structure factors up to the 222 reflection for the reconstruction of the electron density, though they refined six structure factors up to the 331 reflection. It is supposed that they did not use the 331 reflection in order to avoid the appearance of the negative areas in the density map.

4.3. Error introduced by the conversion of crystal structure factors and advantages of electron diffraction to determine electrostatic potential

For obtaining electron density using electron diffraction, we consider the error introduced by the conversion of crystal structure factors for electrons into those for X-rays. The error can be evaluated using the following relation derived from the Mott formula (Watanabe *et al.*, 1969),

$$\left|\frac{\delta f^{\mathrm{X}}}{f^{\mathrm{X}}}\right| = \left|\frac{\delta f^{\mathrm{e}}}{f^{\mathrm{e}}}\right| \frac{Z - f^{\mathrm{X}}}{f^{\mathrm{X}}}, \tag{6}$$

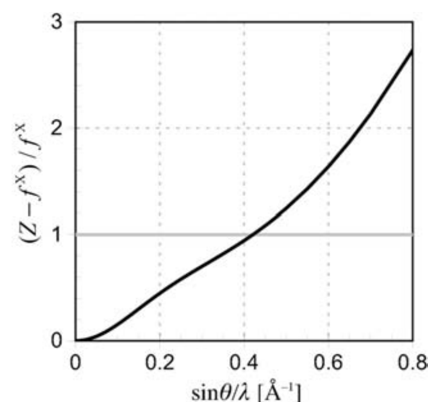

Figure 10
Plot of $(Z - f^{\mathrm{X}})/f^{\mathrm{X}}$ as a function of $\sin\theta/\lambda$.

where f^{X}, f^{e}, δf^{X}, δf^{e} and Z are atomic scattering factors for X-rays and electrons, their estimated errors and the atomic number, respectively. This relation indicates that the relative error $\delta f^{\mathrm{X}}/f^{\mathrm{X}}$ is given by the relative error $\delta f^{\mathrm{e}}/f^{\mathrm{e}}$ multiplied by the factor $(Z - f^{\mathrm{X}})/f^{\mathrm{X}}$. Fig. 10 shows the factor $(Z - f^{\mathrm{X}})/f^{\mathrm{X}}$ for Si as a function of $\sin\theta/\lambda$. The value of $(Z - f^{\mathrm{X}})/f^{\mathrm{X}}$ is seen to be less than 1 in the region of low scattering angles of $\sin\theta/\lambda$ < 0.42 Å^{-1}, which is crucial for accounting for the effect of valence electrons. This implies that in this region the error in the structure factor for X-rays is decreased by the conversion of the structure factor for electrons to that of X-rays. Thus, the electron-diffraction method or CBED is advantageous in the determination of valence electron density. In contrast, the error is increased by the conversion in the region $\sin\theta/\lambda$ > 0.42 Å^{-1}, implying that the refinement of the higher-order structure factors using electron diffraction is less advantageous.

It should be noted that for the determination of the electrostatic potential the Fourier coefficients of the electrostatic potential are directly determined by the CBED method. The electrostatic potential is reconstructed without any errors caused by the conversion of structure factors.

It is also possible to obtain the electrostatic potential from X-ray data inversely using conversion of equation (4). Equation (6), however, shows that the error is increased by the conversion from the structure factors for X-rays to those for electrons in the region of low scattering angles, in which the accuracy of X-ray data is often deteriorated by the extinction effect.

The need to determine the electrostatic potential is increasing. Redistribution of valence electrons, which occurs in the cases of charge ordering, orbital ordering and electronic polarization in various materials, can cause measurable changes in the electrostatic potential distribution. These changes modify the low-order structure factors, which are more sensitive for electron scattering than for X-ray scattering. Electron diffraction or CBED is expected to apply to, for instance, strongly correlated electron materials forming charge- and orbital-ordering and ferroelectric materials accompanied by electronic polarizations.

4.4. Reduction of the number of experimental data points

The influence of the reduction of data points on the accuracy of the refined parameters has been examined. CBED patterns have an enormous number of data points because they are recorded with a very high angular resolution. The reduction of experimental data points is quite efficient for reducing the computation time for dynamical calculations.

Fig. 11(*a*) shows schematic drawings of grids of a CBED disc with pixel-sampling rates of 1/1, 1/9 and 1/36, which are the ratios between the number of pixels of the reduced data and that of the raw data, and Fig. 11(*b*) shows the corresponding experimental patterns. Using the data sets with different pixel-sampling rates, refinements of the Debye–Waller factor, the low-order structure factors and absorption coefficients were performed. Fig. 12 shows the deviation of the Debye–Waller factor refined with the reduced data from the value obtained with the raw data. The deviations are seen to be very small, less than 0.005 Å^2 up to the sampling rate of 1/36. Similarly, Figs. 13(*a*) and 13(*b*) show deviations of the refined Fourier coefficients of the electrostatic potential $V_{\mathbf{g}}$ and absorption potential $V'_{\mathbf{g}}$, respectively, from the values obtained from the raw data. It is also seen that the deviations about $V_{\mathbf{g}}$ are not greater than the standard deviations of the refined values shown in Table 1. These confirm that the structural parameters were successfully refined using 1/16 of the pixels of the raw data without noticeable loss of accuracy.

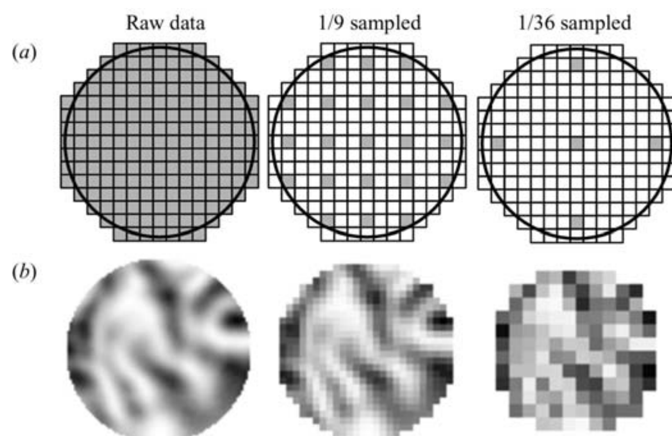

Figure 11
(*a*) Schematic drawings of grids of a CBED disc with different pixel-sampling rates of 1/1, 1/9 and 1/36, and (*b*) corresponding experimental patterns.

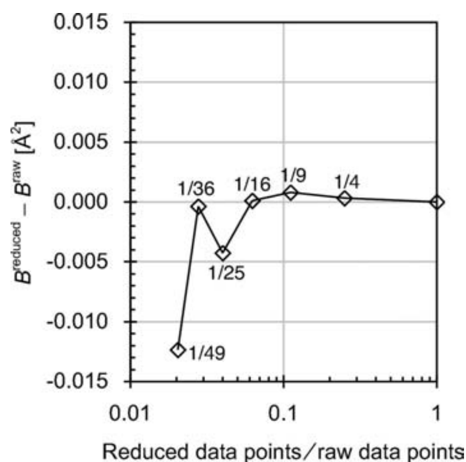

Figure 12
Deviation of the Debye–Waller factor refined with reduced data from the value obtained with the raw data as a function of the ratio between the number of reduced data and that of the raw data.

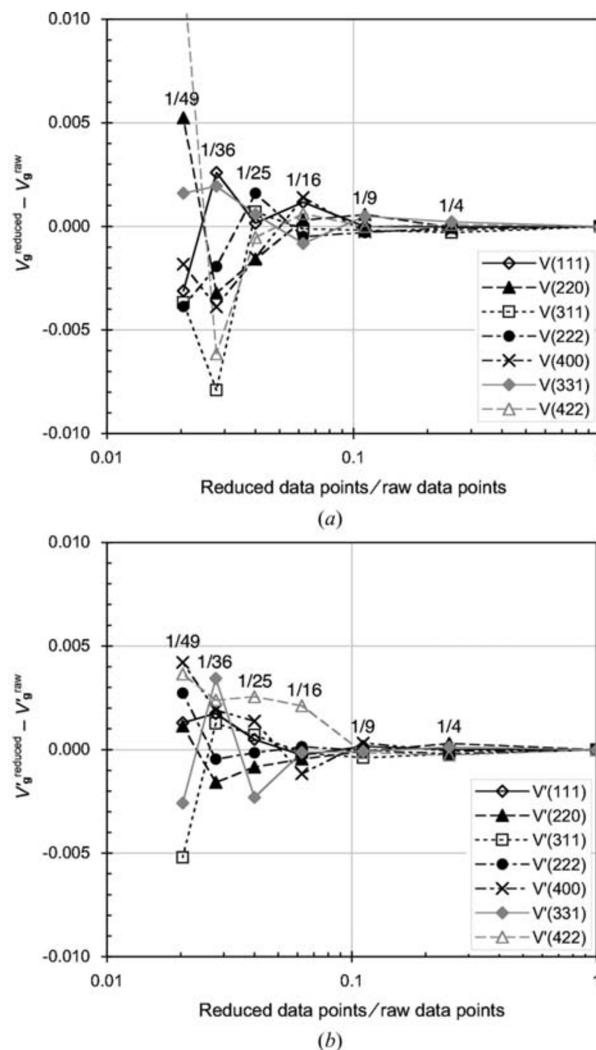

Figure 13
Deviations of the refined Fourier coefficients of the electrostatic potential and absorption potential from those of the raw data as a function of the ratio between the number of the reduced data and that of the raw data.

5. Concluding remarks

We have applied the CBED local structure analysis method developed by Tsuda & Tanaka to crystalline silicon. The Debye–Waller factor of an Si atom and the low-order structure factors and absorption coefficients of the seven reflections with $\sin\theta/\lambda \le 0.451$ Å^{-1} have been accurately determined using only the intensity data of CBED patterns obtained from

specimen areas of a few nanometers in diameter at room temperature. The electrostatic potential and electron density have been reconstructed from the refined parameters with high precision. The latter clearly shows the existence of the bonding electrons between the nearest neighbor atoms. The present study has demonstrated a true nanometer structure analysis using the CBED method.

The influence of the number of refined low-order structure factors on the electron density was examined. The use of multi-CBED patterns recorded with slightly different incidences allows us to refine more numbers of low-order structure factors for minimizing the Fourier truncation errors on the electron densities.

For reducing the calculation time, the experimental data points have been successfully reduced to 1/16 of the raw data without loss of accuracy of the refined parameters in the present analysis. The number of data points is still considerably larger than that of X-ray diffraction experiments. Such a large number of data points are required for expressing the complicated two-dimensional intensity distributions of CBED patterns.

It has been pointed out that, for the determination of the electrostatic potential, CBED is more advantageous than the X-ray method because the Fourier coefficients of the electrostatic potential are directly determined and the electrostatic potential is reconstructed without any errors caused by the conversion from the structure factors for X-rays.

Using the present method of CBED, analyses of the orbital-ordering phase of spinel oxides and ferroelectric perovskite oxides are now under way. This is expected to detect the orbital ordering and electronic polarization in the unit cell, especially through the change of electrostatic potential. Since those materials have minute complex twin domains, the CBED technique is particularly advantageous for obtaining reliable diffraction intensity data from a single domain and for accurately determining the orbital ordering or the ferroelectric polarization.

The authors are grateful to Professor M. Terauchi for helpful discussion and support and Mr F. Satou for his careful maintenance of the JEM-2010FEF. Figs. 5–9 were drawn using the visualization software *VESTA* developed by Mr K. Momma and Dr F. Izumi. The present study was partially supported by a Grant-in-Aid for Scientific Research of the Ministry of Education, Culture, Sports, Science and Technology of Japan.

References

Aldred, P. J. E. & Hart, M. (1973). *Proc. R. Soc. London. Ser. A*, **332**, 223–238.
Becker, P., Seyfried, P. & Siegert, H. (1982). *Z. Phys. B*, **48**, 17–21.
Bird, D. M. & King, Q. A. (1990). *Acta Cryst.* A**46**, 202–208.
Bird, D. M. & Saunders, M. (1992). *Acta Cryst.* A**48**, 555–562.
Cummings, S. & Hart, M. (1988). *Aust. J. Phys.* **41**, 423–431.
Deininger, C., Mayer, J. & Ruhle, M. (1995). *Optik*, **99**, 135–140.
Doyle, P. A. & Turner, P. S. (1968). *Acta Cryst.* A**24**, 390–397.
Fletcher, R. (1971). *A Modified Marquardt Subroutine for Nonlinear Least Squares*, Technical Report R6799. AERE, Harwell, UK.
Friis, J., Jiang, B., Marthinsen, K. & Holmestad, R. (2005). *Acta Cryst.* A**61**, 223–230.
Friis, J., Jiang, B., Spence, J., Marthinsen, K. & Holmestad, R. (2004). *Acta Cryst.* A**60**, 402–408.
Hall, C. R. & Hirsch, P. B. (1965). *Proc. R. Soc. London Ser. A*, **286**, 158–177.
Ichikawa, M. & Hayakawa, K. (1977). *J. Phys. Soc. Jpn*, **42**, 1957–1964.
Jiang, B., Zuo, J. M., Jiang, N., O'Keeffe, M. & Spence, J. C. H. (2003). *Acta Cryst.* A**59**, 341–350.
Momma, K. & Izumi, F. (2008). *J. Appl. Cryst.* **41**, 653–658.
Nishibori, E., Sunaoshi, E., Yoshida, A., Aoyagi, S., Kato, K., Takata, M. & Sakata, M. (2007). *Acta Cryst.* A**63**, 43–52.
Ogata, Y., Tsuda, K., Akishige, Y. & Tanaka, M. (2004). *Acta Cryst.* A**60**, 525–531.
Rees, B. (1978). *Acta Cryst.* A**34**, 254–256.
Saka, T. & Kato, N. (1986). *Acta Cryst.* A**42**, 469–478.
Saunders, M., Bird, D. M., Holbrook, O. F., Midgley, P. A. & Vincent, R. (1996). *Ultramicroscopy*, **65**, 42–52.
Saunders, M., Bird, D. M., Zaluzec, N. J., Burgess, W. G., Preston, A. R. & Humphreys, C. (1995). *Ultramicroscopy*, **60**, 311–323.
Saunders, M., Fox, A. G. & Midgley, P. A. (1999*a*). *Acta Cryst.* A**55**, 471–479.
Saunders, M., Fox, A. G. & Midgley, P. A. (1999*b*). *Acta Cryst.* A**55**, 480–488.
Spackman, M. A. (1986). *Acta Cryst.* A**42**, 271–281.
Spence, J. C. H. (1993). *Acta Cryst.* A**49**, 231–260.
Spence, J. C. H. & Zuo, J. M. (1992). *Electron Microdiffraction.* New York: Plenum.
Streltsov, V. A., Nakashima, P. N. H. & Johnson, A. W. S. (2003). *Microsc. Microanal.* **9**, 419–427.
Tanaka, M., Tsuda, K., Terauchi, M., Tsuno, K., Kaneyama, K., Honda, T. & Ishida, M. (1999). *J. Microsc.* **194**, 219–227.
Teworte, R. & Bonse, U. (1984). *Phys. Rev. B*, **29**, 2102–2108.
Tsuda, K., Ogata, Y., Takagi, K., Hashimoto, T. & Tanaka, M. (2002). *Acta Cryst.* A**58**, 514–525.
Tsuda, K. & Tanaka, M. (1999). *Acta Cryst.* A**55**, 939–954.
Watanabe, D., Uyeda, R. & Fukuhara, A. (1969). *Acta Cryst.* A**25**, 138–140.
Yamamoto, K., Takahashi, Y., Ohshima, K., Okamura, F. P. & Yukino, K. (1996). *Acta Cryst.* A**52**, 606–613.
Zuo, J. M. (2004). *Rep. Prog. Phys.* **67**, 2053–2103.
Zuo, J. M., Blaha, P. & Schwarz, K. (1997). *J. Phys. Condens. Matter*, **9**, 7541–7561.
Zuo, J. M., Kim, M., O'Keeffe, M. & Spence, J. C. H. (1999). *Nature (London)*, **401**, 49–52.